Fracture Analysis of Tube-gusset-intersecting Joint Based on SWDM Microscopic Fracture Mechanism

Rujie Deng [1,*], Xianqiao Meng[2], Shulin Zhang[2], and Zhengliang Li[1,3]

[1] College of Civil Engineering, Chongqing University, Chongqing, China
[2] China Energy Engineering Group Anhui Electric Power Design Institute Co., LTD., Anhui, China; Email: zhangsl@ahedi.com.cn (S.Z.)
[3] Key Laboratory of Construction and New Technology of Mountainous Region Cities, Chinese Ministry of Education, Chongqing University, Chongqing, China; Email: lizhengliang@hotmail.com (Z.L.)
*Correspondence: dengrujie_edu@163.com (R.D.)

***Abstract*—The Stress-weighted Damage Model (SWDM) based on microscopic fracture mechanism can be used to predict the ductile fracture of steel by considering the influence of lode angle parameters and stress triaxiality. However, the calibration work of undetermined parameters of this model is not perfect, especially for Q420C steel is rarely reported. In addition, the fracture analysis using the microscopic fracture mechanism model is still mainly focused on simple structure, and the analysis of complex joint is rarely reported. In this study, the parameters of SWDM model of Q420C and Q355B steel were calibrated through the material test and finite element analysis. The constitutive model based on SWDM was realized by ANSYS program, and the influence of model mesh size was considered. Then, the fracture analysis of a new type KT joint with both tube-gusset and intersecting connections was carried out. The analysis results show that for the connecting plate of the oblique branch pipe of the joint, the cracks first appear at the end of the connecting plate on the outside and the edge of the ring plate, then the cracks gradually expand and connect with the cracks near the bolt holes. Finally, the cracks extend to the horizontal circular pipe and tear the connecting plate from the horizontal circular pipe. In the process of loading, the influence of horizontal and vertical circular pipe axial force on the ultimate bearing capacity of inclined branch pipe is only 4%, which is relatively limited. In addition, the bearing capacity of the node can still be increased by about 16% after the crack appears, which means that the joint has great guarantee of security.**

***Keywords*—microscopic fracture mechanism, parameter calibration, tube-gusset-intersecting joints, post fracture path**

I. Introduction

With the increasing requirements of engineering Structures, including Ultra High Voltage (UHV) transmission towers, on the complexity and bearing capacity of joint connections, the traditional intersecting joints can no longer meet the requirements. Therefore, scholars all over the world have studied different connection methods of intersecting joints. For example, Yang [1] conducted research on T-shaped tubular joints strengthened with annular plates, and Qu [2] conducted experimental analysis on X-shaped joints strengthened with annular plates at the ends of connecting plates. Li [3] used gusset plates and annular stiffeners to strengthen the cross type intersecting joints, and completed test and finite element analysis.

Although a lot of useful exploration has been carried out, the relevant research is still insufficient. The research of reinforced steel pipe joints is still mainly aimed at the joints with only tube plate connection or only intersecting connection. Up to now, there are few research reports on the joint forms that use two types of connection structures at the same time, and the failure form of this type of joint is not sufficiently studied. Therefore, it is necessary to analyze the joint failure stage in detail to clarify its final failure form and safety reserve range.

Since traditional fracture mechanics need to assume the existence of initial cracks and the existence of high strain constraints at the tip of initial cracks, it is not applicable to ductile fracture problems without obvious defects and with large-scale yielding [4]. However, the fracture model based on micromechanism can accurately predict the ductile fracture without obvious initial crack due to large-scale yield by describing the influence of stress-strain field on the internal microstructure of materials [5]. Based on this, scholars have made a lot of analysis. Ric and Trace [6] proposed an exponential relationship between void growth and stress triaxiality, and then proposed a Void Growth Model (VGM). Kanvinde [7] proposed a Cyclic Void Growth Model (CVGM) for reciprocating loads on the basis of VGM model. On the basis of CVGM model, Smith *et al.* [8] modified the model by taking into account the influence of lode angle parameter parameters and proposed a Stress-Weighted Damage Model (SWDM). Up

Manuscript received December 14, 2022; revised January 25, 2023; accepted February 5, 2023.

doi: 10.18178/ijscer.12.3.76-84

to now, the relevant theories have become mature and many scholars have begun to apply them to engineering. For example, Chen [9] used the VGM model to predict the fracture of test specimens made of Q345 steel and carried out post crack path tracking analysis. Yin [10] used the VGM model and Stress Modified Critical Strain (SMCS) model to predict the fracture of XK type intersecting joints. Up to now, VGM and SMCS models are still the main models for ductile fracture prediction under monotonic loads in engineering structures, while the fracture model considering lode angle parameter is seldom used [11].

Based on the situation mentioned above, this study analyzed the bearing capacity limit state of a new type of UHV transmission tower tube-gusset-intersecting joint, and used an improved SWDM microscopic fracture mechanism model to calculate the effect of lode angle parameter. The parameters of SWDM model of Q420C steel used for UHV transmission tower were calibrated through tests, and the fracture model was imported into the ANSYS program. In this study, the monotonic loading analysis was carried out on the joints, and the failure mode of cracking and path expansion after cracking was predicted. It is expected to provide a reference for the research of bearing capacity of this kind of joints.

II. Theoretical Basis of SWDM Model for Micro Fracture Mechanism

Smith *et al.* [8] proposed a stress-weighted damage model (SWDM) by introducing lode angle parameter term into CVGM model to consider the effect of lode angle, and using hyperbolic sine function to express stress triaxiality. The damage variable increment dD is shown in Eq. (1).

$$\mathrm{d}D = C(e^{A^{+}T} - e^{-A^{-}T})e^{k\xi} d\bar{\varepsilon}_p \tag{1}$$

$$\xi = \cos(3\theta) = \frac{3\sqrt{3}J_3}{2J_2^{3/2}} \tag{2}$$

where C, A^+, A^-, k are the undetermined parameters related to materials, which can be obtained through calibration and calculation through test; T is the stress triaxiality; $d\bar{\varepsilon}_p$ is the equivalent plastic strain increment; ξ is the lode angle parameter; θ is the lode angle; J_2, J_3 is the second and third invariants of deviatoric stress tensor respectively. When the D value is integrated to 1, the material starts to fracture.

Chen *et al.* [11], referring to the relationship between CVGM and VGM models, improved the SWDM model for monotonic loading. The incremental form of damage variable D is show in Eq. (3).

$$\mathrm{d}D = C\, e^{AT} e^{k\xi} d\bar{\varepsilon}_p \tag{3}$$

where the meaning of A is analogous to that of A^+ and A^- in Eq. (1), and other parameters are consistent with (1). In this study, the monotonic loading analysis is carried out for the joints, so Eq. (3) is used to modify the finite element constitutive model and conduct fracture analysis.

III. SWDM Parameter Calibration Test Design

As there are few fracture model calibration tests for the steel Q420C and Q355B used for UHV transmission tower, especially the tests designed for SWDM model considering lode angle parameters are rarely reported, this study referred to the experiments of Chen *et al.* [11], designed and manufactured a batch of test specimens to complete the calibration of model parameters.

In this study, 6 kinds of test specimens were designed. Two groups of each kind of test specimens were made according to Q420C and Q355B. The size and quantity of each test specimen are shown in Figs. 2–7. SRB is a smooth round bar with a central diameter of 6 mm. RBGA and RBGB are notched round bar test specimens with notched radius of 2 mm and 5 mm, respectively. PWGA and PWGB are notched grooved plate test specimens with notch radii of 3 mm and 6 mm, respectively. STP is a shear tensile test piece with a deflection angle of 45°, and the width and thickness of the notch center is 6 mm. All test specimens were sampled from the middle of complete Q420C and Q355B steel plates, sampled by wire cutting and cooled by water during the cutting process. At the same time, more than 20 mm was reserved between the test specimen and the steel plate edge to reduce the impact of processing on the material properties of the sample.

In this study, the INSTRON material test 1342 system was used to carry out monotonic tensile loading on the test specimen. During the loading process, the load data was recorded by the sensor at the supporting end, and the displacement data of the test specimen was recorded by the electronic extensometer.

Figure 1. Test loading device.

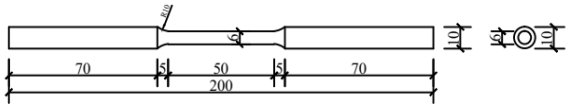

Figure 2. Material properties test piece SRB.

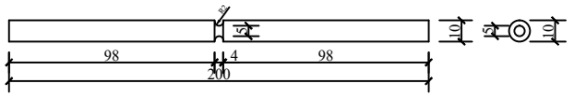

Figure 3. Notched round bar test specimen RBGA.

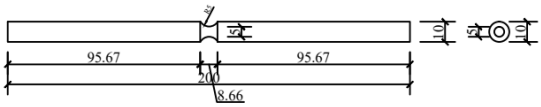

Figure 4. Notched round bar test specimen RBGB.

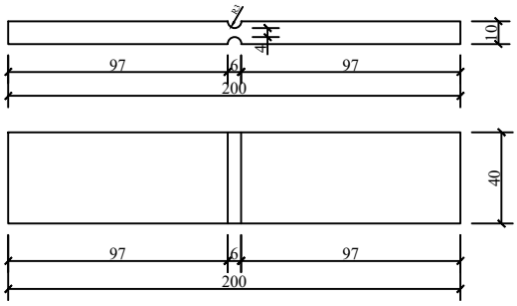

Figure 5. Notched groove plate test specimen PWGA.

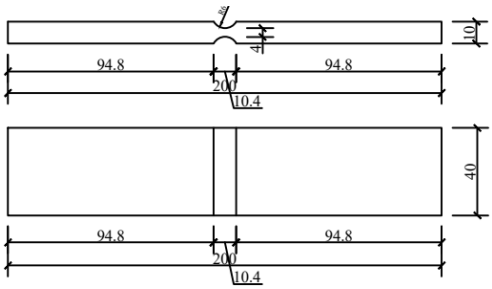

Figure 6. Notched groove plate test specimen PWGB.

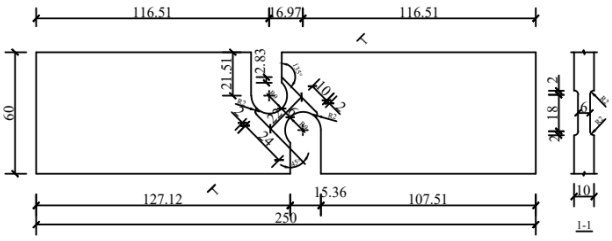

Figure 7. Shear and tension test specimen STP.

IV. Test Results and Finite Element Analysis

A. Monotonic Tensile Test of Material Properties

The SRB of the smooth round bar test specimens were loaded to determine the basic mechanical parameters of the material. Due to the necking phenomenon of the test specimen in the late loading period, this study only processed the load and displacement readings before necking and obtained the engineering stress and strain by using Eqs. (4) and (5). Then, Eqs. (6) and (7) were used to correct the engineering stress and strain, and the true stress (σtrue) and true strain (εtrue) of the material before necking were obtained.

$$\sigma_0 = \frac{F}{A_0} \tag{4}$$

$$\varepsilon_0 = \frac{\Delta L}{L_0} \tag{5}$$

$$\sigma_{\text{true}} = \sigma_0(1+\varepsilon_0) \tag{6}$$

$$\varepsilon_{\text{true}} = \ln(1+\varepsilon_0) \tag{7}$$

where, F is the measured load value at the loading end, A_0 is the measured original section area of the test specimen's standard distance section, ΔL is the change value of the standard distance section length, L_0 is the original length of the standard distance section.

In order to obtain the real stress-strain curve of the material after necking, it is necessary to extrapolate the data reasonably. The MWA method proposed by Jia [12] was adopted in this study, and the true stress-strain curve after necking was defined as Eq. (8).

$$\sigma_{\text{true}} = \sigma_n + w\sigma_n(\varepsilon_{true} - \varepsilon_n) \tag{8}$$

where, σ_n and ε_n is the real stress and strain at the moment of necking; w is the weighting factor. By comparing the simulated loading curve and the test curve, test algorithm is used to calibrate the value of w. In this study, the real stress-strain curves of Q420C and Q355B steel are drawn by the above method, as shown in Fig. 8.

B. Monotonic Tensile Test and Finite Element for Notched Test Specimens

According to the geometric symmetry characteristics, the models were set up with 1/4 or 1/2 to simplify the calculation. The weakened part of the sample was divided by grids with a size of 0.2 mm, which corresponded to the characteristic length of the material [13]. By setting enough loading steps, the increment of damage variable calculated each time was small enough to provide sufficient integration accuracy. The slope mutation point of the test load displacement curve or the end point of the curve data was taken as the fracture point of the test specimen, and the corresponding fracture displacement was applied to the test specimen as the finite element displacement load.

RBGA and RBGB series test specimens have no obvious deformation during loading, and the test specimens were nearly instantaneous failure. The fracture was located at the minimum net section, and the failure was uneven, with many grooves and bumps.

During the loading process of PWGA and PWGB series test specimens, the minimum section was significantly dented along the long side. During the failure, the crack started at the center of the section and rapidly expanded to both sides, resulting in a rapid reduction of the bearing capacity, and then the test was terminated. At this point, some test specimens were completely disconnected, while others were still connected in small amounts at the edges. The test specimen fracture was fibrous, and the fracture was rough but relatively smooth.

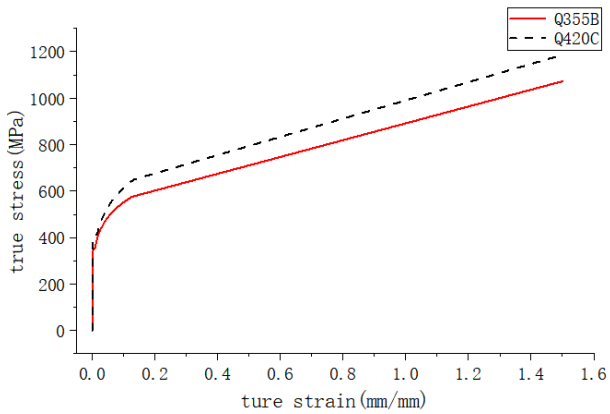

Figure 8. True stress-strain curves of materials.

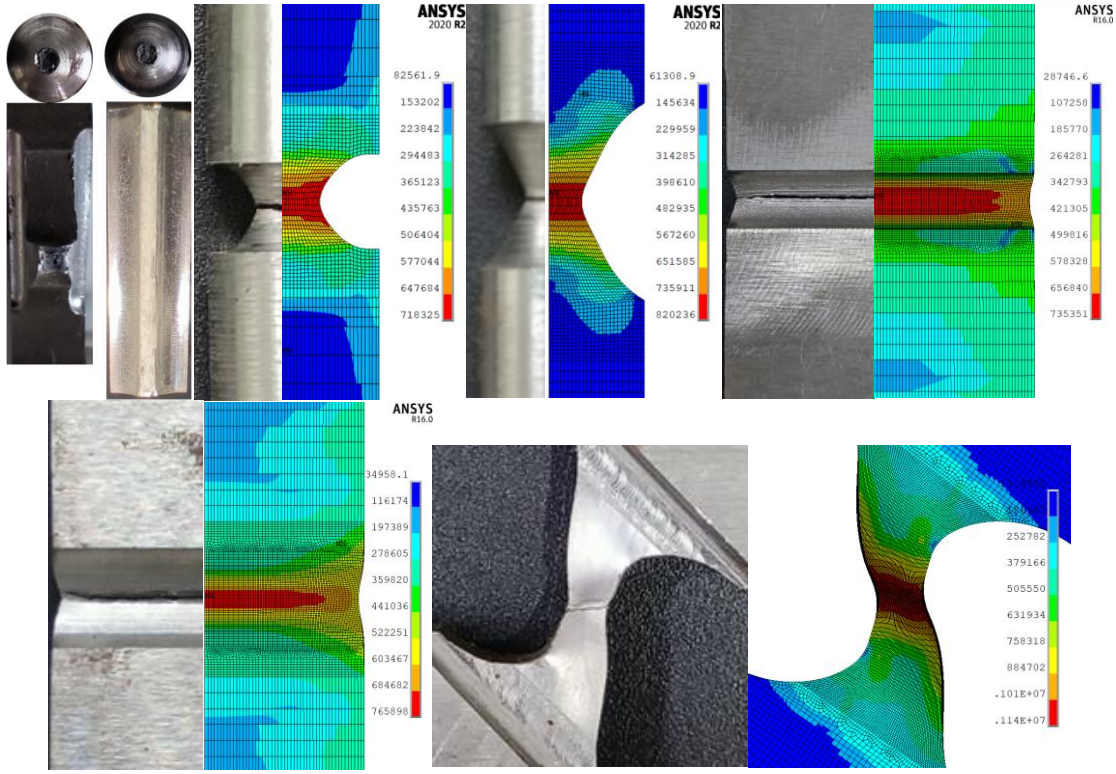

Figure 9. Failure patterns of test specimen fracture and corresponding finite element results.

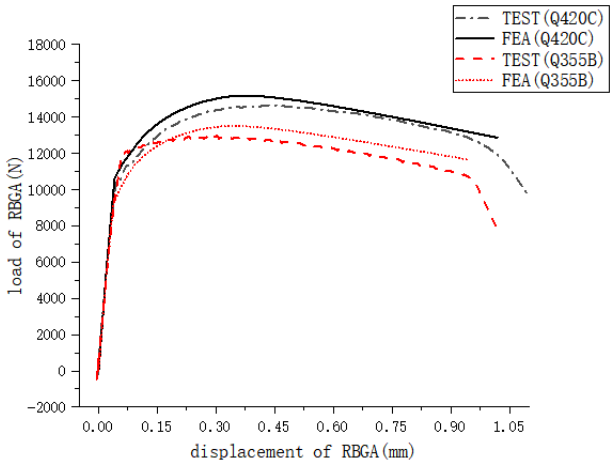

Figure 10. Test and finite element loading curve of RBGA.

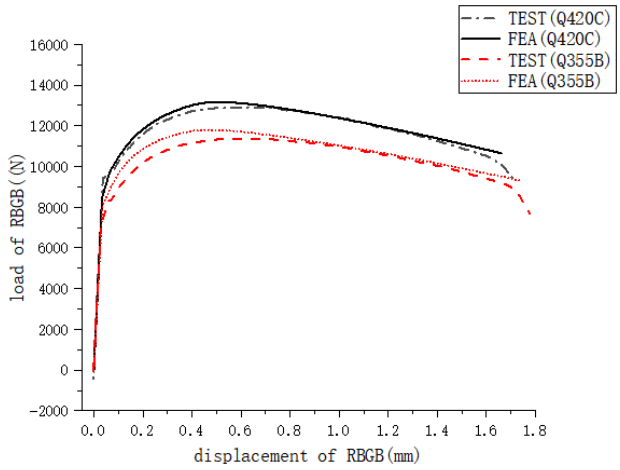

Figure 11. Test and finite element loading curve of RBGB.

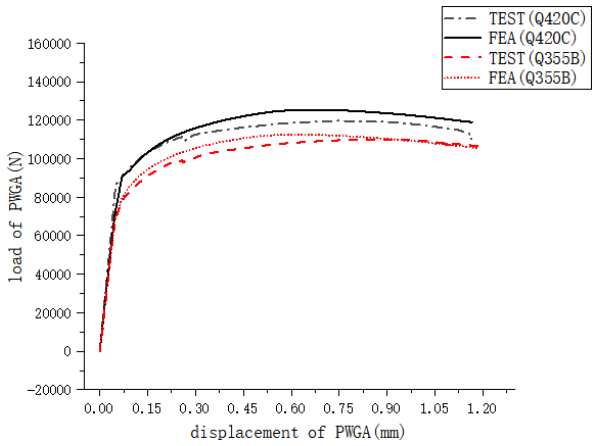

Figure 12. Test and finite element loading curve of PWGA.

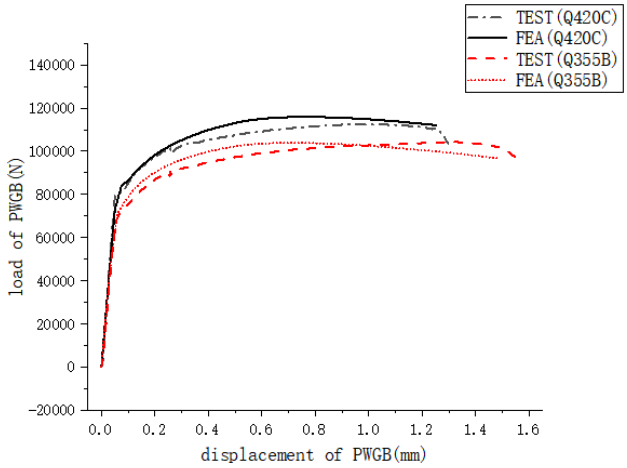

Figure 13. Test and finite element loading curve of PWGB.

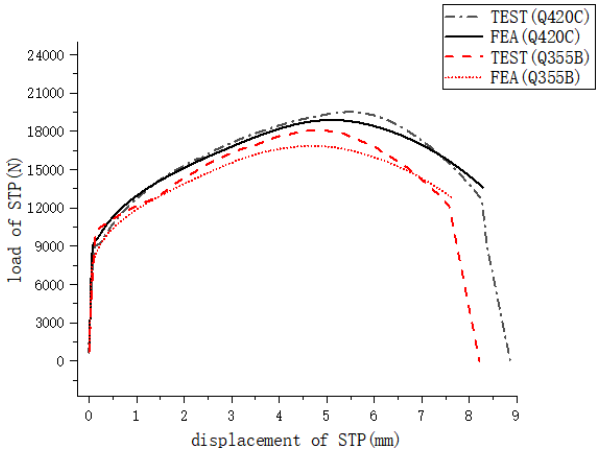

Figure 14. Test and finite element loading curve of STP.

During the loading process of STP series test specimens, obvious deformation occurred in the core region, and gradually changed from the 45° shear tension state to the axial tensile state during the loading process, and eventually the core area was pulled off instantaneously. After loading, the test specimens have obvious plastic deformation.

C. Calibration of SWDM Fracture Parameters

Small loading increments were selected during the loading process of the test specimen, and the parameters such as stress triaxiality, equivalent plastic strain and lode angle were recorded. The coefficients in the fracture parameters were taken as unknowns, and the cumulative value of damage variables corresponding to the end of fracture displacement loading was taken as 1, so as to establish the undetermined coefficient equation of SWDM model. According to the principle of least square method, using MATLAB program to fit the results of multiple groups of experiments to determine the final coefficient value. SWDM model parameters of Q420C and Q355B steel obtained after calibration are shown as Table I. Chen [14] calibrated Q460C steel and obtained the fracture parameters as C=0.546, A=1.245, K = −0.193, respectively. Combined with previous achievements, Chen [15] pointed out that the value range of C is [0.25,1], and the value of A is [0,2]. When Smith [8] proposed the SWDM model, he pointed out that the value of k could be positive or negative, with a wide range. Therefore, the parameters obtained by calibration for Q420C and Q355B in this study are within a reasonable range and conform to the relevant physical significance.

V. Joint Fracture Analysis Based on SWDM

A. Joint and Finite Element Model Description

The intersecting joint in this study is a planar KT joint, and its structure is shown on the left in Fig. 15. The horizontal branch pipe adopts intersecting connection, and the oblique branch pipe adopts tube-plate connection. In addition, the joints are strengthened with a plurality of ring stiffening plates. The main pipe radius is 482.5 mm and the thickness is 38 mm; the branch pipe radius is 254 mm and the thickness is 10 mm; the upper and lower connecting plates are 22 mm and 24 mm, respectively; the outer diameter of the horizontal stiffening plate is 682.5 mm and the thickness is 16 mm. The outermost ring plate is a simplified flange, and the higher material strength and strengthening measures of the flange plate is considered by giving higher material strength. According to the experimental calculation, the fracture of the joint mainly occurs on the connecting plate and the wall of the branch pipe. Therefore, considering the joint size, the grid size of 8 mm was adopted for the joint plate and the branch pipe, and relatively large grid size was adopted for the other areas. The lower end of the main joint was subject to fixed constraints. The end of the horizontal branch pipe and the upper end of the main pipe were considered as sliding supports to restrict the tangential displacement while retaining the axial freedom. The inclined branch pipe was connected by bolts in structure. According to the research conclusion of Shen [16], the branch pipe was simplified, only the part of bolt connecting plate and part of bolt connected to the joint was considered, and the displacement load was directly imposed on the section of bolt connecting plate. The simplified joint is shown on the right of Fig. 15.

B. Finite Element Realization of Post-crack Path Analysis

Liao [17] used the self-programmed ABAQUS program to define the units that reached the fracture criterion in the loading analysis process as failure and deleted them one by one. Through the above method, Liao [17] completed the post-fracture path analysis for ductile faults, and determined the post-fracture load displacement curve. However, this simulation method requires the element size to be limited to the material characteristic size scale (about 0.2 mm), which is often unacceptable for the finite element analysis of normal steel structural members. Yin [18], referring to the idea of continuous damage mechanics, proposed a computational model considering the criterion of material continuous damage.

TABLE I. Calibrated Fracture Parameters

	C	A	K
Q420C	0.5049	1.4229	-0.2020
Q355B	0.4282	1.4524	-0.0432

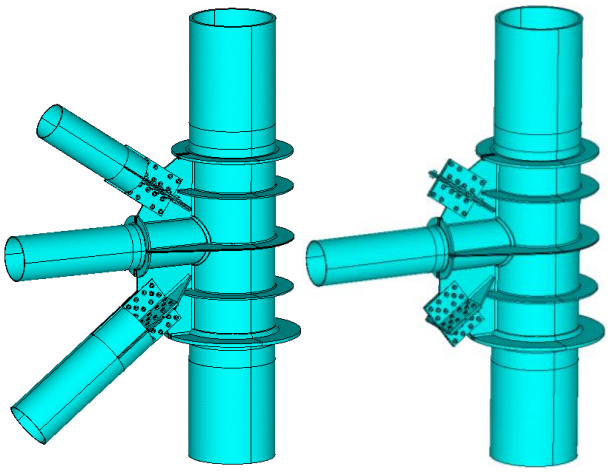

Figure 15. Complete joints and computationally simplified joints.

At the same load level, models with different mesh sizes should be subjected to the same ductile fracture damage. Therefore, the model assumes that large mesh cells will experience a partial fracture state between the initiation of fracture and complete fracture. In this state, the crack will continue to expand in the element. In the finite element calculation, this state is simulated by reducing the element stiffness, namely the elastic modulus, to ensure that the damage of the structure is the same under different meshing conditions. According to the formula proposed by Yin [18], the stiffness reduction coefficient of the material model is calculated as shown in Eq. (9).

$$E = E_0(1 - D_{lost})^n \tag{9}$$

where, E_0 is the unmodified elastic modulus of the material; E is the elastic modulus of the material after partial reduction; D_{lost} is the damage coefficient; n is the exponential term related to the size of the grid.

$$D_{lost} = (D - D_0)/(1 - D_0) \tag{10}$$

where, D_0 is the threshold value of crack initiation; when the element fracture parameter D is less than D_0, the material is in a state of uncracked; when D_0 is reached, the material begins to fracture ($0 < D_{lost} < 1$); thereafter, the material is in a state of damage reduced by the elastic model; when D is greater than 1, the material element completely fails and is deleted in the finite element network. The calibration of D_0 firstly calculates the small-size mesh model to determine the crack initiation position and the load level at this time. Then the large-size mesh is used to load at the same load level, and D value corresponding to the element of the large-size mesh at the crack initiation position is the threshold value D_0. For the other parameters in the formula, Yue Yin [18] gave the reference formula as shown in Eqs. (11) and (12).

$$n = -120P + 120 \tag{11}$$

$$P = \varepsilon_P^{CM} / \varepsilon_P^{FM} \tag{12}$$

where, n is mainly affected by the size and shape of the large size cell grid. ε_P^{CM} and ε_P^{FM} are the equivalent plastic strain of the element at the initial position of fracture under the initiation load of large and small mesh division respectively.

In this study, the initial fracture position of the joint was determined by the trial calculation, and then the mesh here was refined to the characteristic length of steel of 0.2 mm. The stiffness reduction coefficient parameters of the large mesh elements were calibrated and calculated, and the results are shown in Table II. Since the material properties are not changed during the calibration process, the sub-model and the duple sub-model technology can be used to refine the local results, which makes the calculated amount in the calibration process not increases significantly.

Considering that the material properties will change in the calculation process, and the structure will produce great nonlinear deformation, it will be difficult to converge the results calculated by using ANSYS implicit analysis. Therefore, the explicit dynamic analysis module ANSYS/ls-dyna was used in this study to analyze the fracture of the joint, and a long enough loading step was set for quasi-static loading to avoid the influence of dynamic effects. Through APDL command flow, the above calculation content was taken into account to realize the finite element analysis of SWDM model considering damage. The concrete implementation process of finite element calculation is shown in Fig. 16.

C. Finite Element Calculation Results of Joints

Since the dimensions of the round tube are the same inside and outside the joint domain, and the joints have taken various reinforcement measures, the failure should occur outside the joint domain when only the axial force is applied to the round tube. Therefore, this study adopted the load method of applying equal large reverse axial displacement load to the section of the upper and lower inclined pipe connecting plate, and the load gradually increases from 0 to joint failure.

In order to study the influence of axial force on the failure of steel pipe joints, four working conditions were designed by changing the horizontal and vertical axial forces of joints. Working condition 1 is to impose no axial force on the horizontal and vertical circular pipe, working condition 2 is to impose 4000 KN additional horizontal axial force, working condition 3 is to impose 10000 KN additional vertical axial force, and working condition 4 is to impose both horizontal and vertical axial force. The calculation results of crack germination and growth under four working conditions are shown in Figs. 17–20, and the load displacement curve of inclined branch connecting plate is shown in Figs. 21 and 22.

TABLE II. COEFFICIENT FOR DAMAGE CALCULATION

	D_0	n
Q420C	0.28229	76.002
Q355B	0.49318	64.874

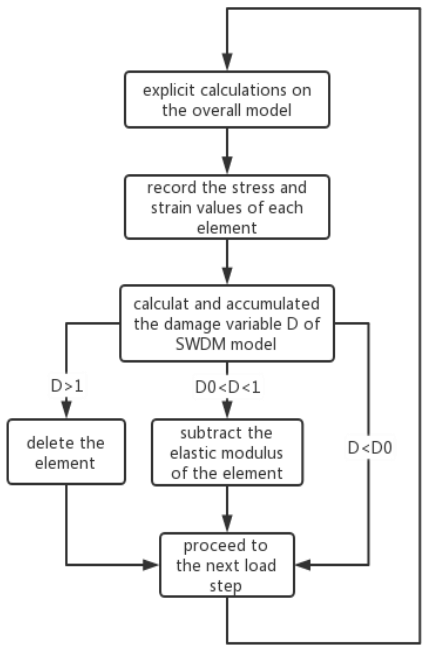

Figure 16. Finite element calculation flow chart.

By calculating the joints without horizontal and vertical axial forces, we found that the crack first started from the end of the outer connecting plate on the lower side, but after the crack extended to the whole end face, the crack did not continue to expand for a long time. As the load continued to increase, cracks also appeared at the junction of the outer connecting plate on the lower side and the ring plate on the lower side. Subsequently, the cracks rapidly expanded to the corner bolt hole and connected with the cracks at the bolt hole, and the bearing capacity of the lower connecting plate decreased rapidly. During the process of crack penetration, the initial crack also began to propagate towards the branch pipe along the vertical load direction. The crack then spread upward to the weld between the horizontal branch pipe and the connecting plate, and spread rapidly along the weld, causing the connecting plate to tear from the branch pipe. The destruction process is shown in Fig. 17.

Considering the symmetry of the failure site of the upper connecting plate, the failure of the upper connecting plate was almost unaffected by the horizontal and vertical loads. For the lower connecting plate, the crack growth angle was slightly different under different loads, but the general trend of crack growth and the failure mode of the structure were not significantly affected by the load. The crack of the lower connecting plate still started from the end of the plate, but the propagation speed was faster than that of the condition without axial force. In addition, the direction of the crack propagation was vertical upward, which was different from the oblique direction of vertical load propagation under the condition without axial force. The crack extended to the branch pipe and then teared the connecting plate from the branch pipe along the weld direction. The destruction process is shown in Figs. 18–19.

When the horizontal and vertical axial forces were applied at the same time, the crack development mode of the upper connecting plate had no obvious change. The crack of the lower connecting plate still germinated from the end of the lateral connecting plate, spread down to the bolt to form a through crack, and spread upward to the horizontal branch pipe. However, when the crack continued to propagate in the branch pipe, the crack propagation mode was different from that along the weld in other working conditions. In the working condition 4, the crack growth path gradually curved upward and away from the weld, eventually tearing the branch wall along the inclined direction. The destruction process of working condition 4 is shown in Fig. 20.

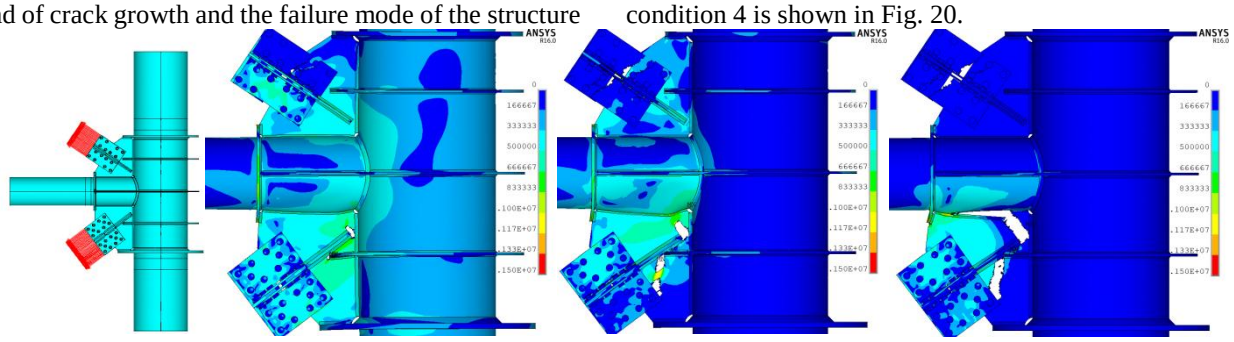

Figure 17. Failure mode under working condition 1.

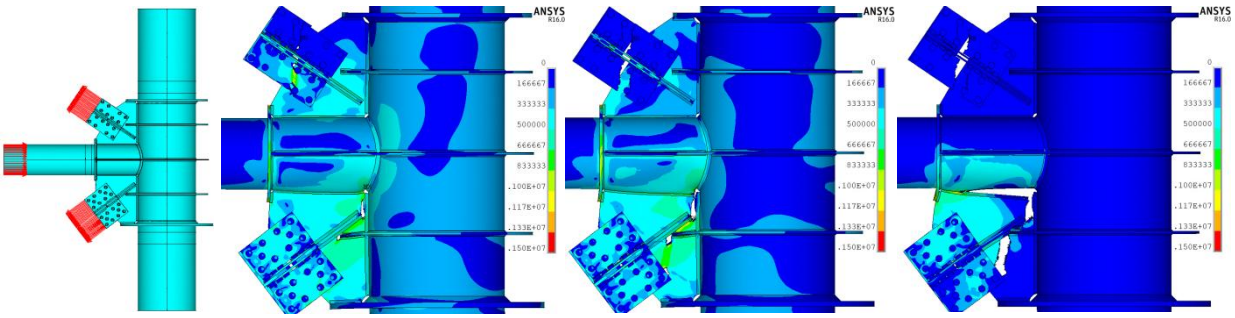

Figure 18. Failure mode under working condition 2.

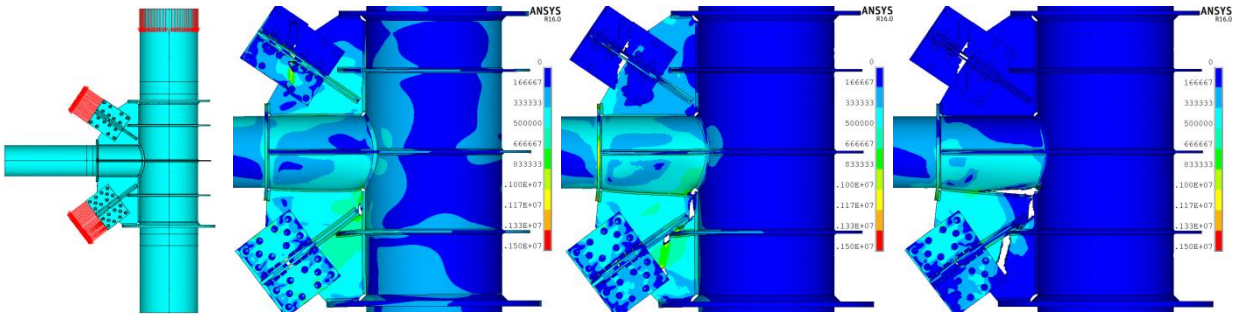

Figure 19. Failure mode under working condition 3.

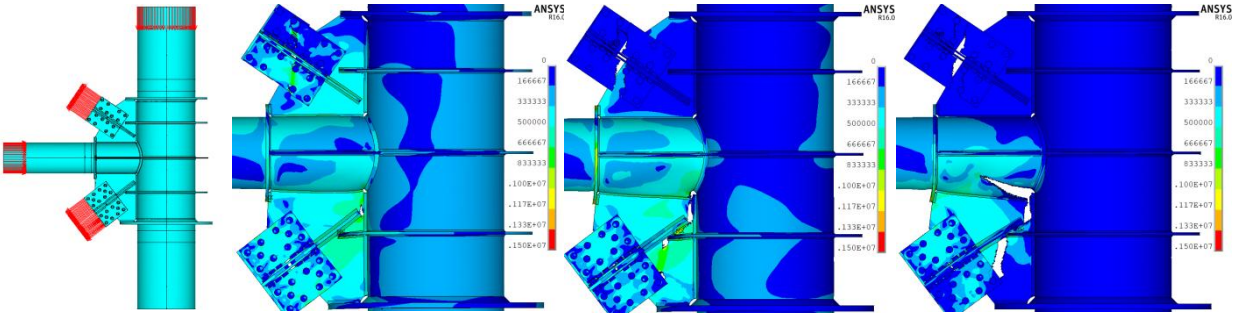

Figure 20. Failure mode under working condition 4.

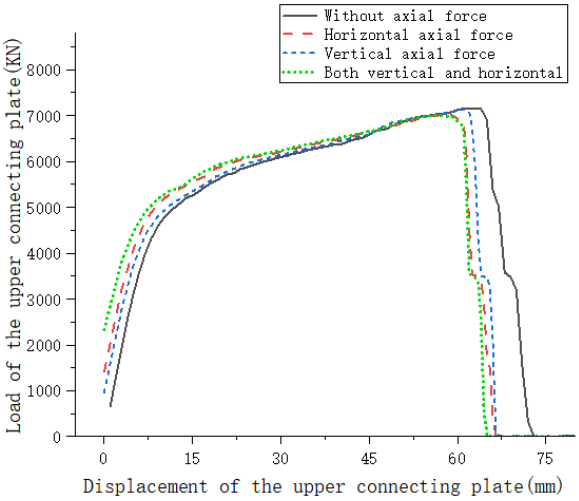

Figure 21. The load-displacement curve of upper oblique branch pipe.

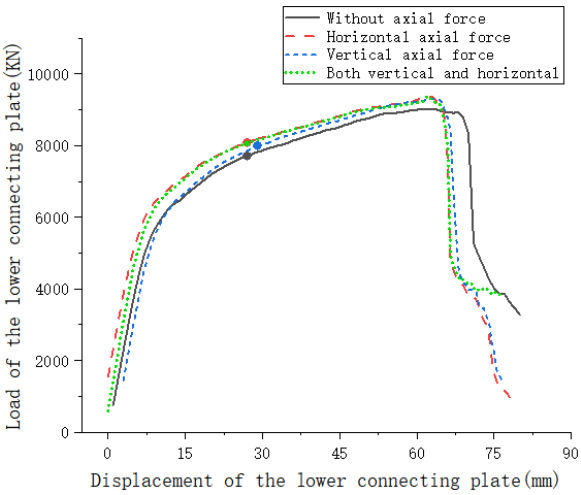

Figure 22. The load-displacement curve of the lower oblique branch pipe.

Extracting the load displacement curves under four working conditions we can see that the horizontal and vertical axial forces do not change the overall shape of the load displacement curves of the inclined connecting plates. Only in the latter half of the fracture development stage of working condition 4, the curve shape changes compared with the other three working conditions, which is consistent with the characteristics of failure forms in each working condition mentioned above.

The value of ultimate bearing capacity of oblique branch pipe was also read out, and the variation amplitude of ultimate bearing capacity of other working conditions relative to working condition 1 was calculated, which is listed in Table III. It can be seen that the bearing capacity of inclined branch pipe varies less than 4% under the influence of axial force, which is relatively small.

In addition, after the horizontal or vertical axial forces were applied to the joints, the inclined connecting plates reached the ultimate load earlier and fracture earlier, which may be caused by the fact that the connecting plates formed more adverse stress and reached the fracture criterion faster. The ultimate bearing capacity of the upper connecting plate decreased, while the ultimate bearing capacity of the lower connecting plate increased to a certain extent. The reason might be that the upper fractured connecting plate had a simple structure, and failure occurred immediately after the stress was unfavorable. However, due to the many reinforced structures on the lower side of the fractured connecting plate, the unfavorable stress drove the surrounding members to have greater collaborative deformation, so the overall bearing capacity was increased.

The data point at the beginning of material fracture in the joint loading was also recorded, which is highlighted in the load displacement curve of the lower connecting plate in this study. It can be seen that the initial crack appeared when the displacement load of the joint reached about 30 mm, but after that, the bearing capacity of the joint still improved significantly with the progress of loading, and the joint did not reach the maximum bearing capacity and completely failed until it continued to undergo plastic deformation of about 30 mm displacement loading. The load value corresponding to the initial crack of the node and the remaining strength at this time are listed in Table IV. It can be seen that for this joint, the appearance of cracks does not mean that the joint fails completely. At this time, the bearing capacity can still be increased by about 16%, which means that the joint has a large safety reserve.

TABLE III. ULTIMATE BEARING CAPACITY OF OBLIQUE BRANCH PIPE

	value of the upper side	variation value	value of the lower side	variation value
Working condition 1	7162KN	0	9030KN	0
Working condition 2	7007KN	2.16%	9369KN	3.75%
Working condition 3	7111KN	0.71%	9305KN	3.05%
Working condition 4	7000KN	2.26%	9387KN	3.95%

TABLE IV. INITIAL FRACTURE LOAD OF LOWER OBLIQUE BRANCH PIPE

	Fracture load value	Residual bearing capacity	Residual bearing capacity ratio
Working condition 1	7713KN	1317KN	17.08%
Working condition 2	8088KN	1281KN	15.84%
Working condition 3	7998KN	1307KN	16.34%
Working condition 4	8063KN	1324KN	16.42%

VI. CONCLUSION

(1) The material parameters of Q420C and Q355B steel in micro-fracture mechanism SWDM were calibrated through 12 sets of axial tensile tests and finite element analysis, which can provide data reference for similar models and fill the gap of relevant data.

(2) The SWDM model was successfully implemented in the finite element calculation in this study, and the post-fracture path analysis was carried out for the new tube-gusset-intersecting joint and the load displacement curve was obtained, which provided ideas and references for the fracture analysis of this kind of complex structure.

(3) The horizontal and vertical axial forces of this kind of joint have limited influence on the load displacement curve, the post-crack path development and the failure mode of the inclined joint plate. The maximum influence range on the peak carrying capacity is 4%, which is still small.

(4) For the joints with complex structures and multi-channel stiffened plates, the appearance of cracks does not mean that the joints have reached the ultimate bearing capacity. The bearing capacity of the joints can still be increased by about 16%, indicating that the joints have a large safety surplus.

(5) In this study, only the failure condition of monotone loading is analyzed. In the future, the failure condition of ultra-low cycle fatigue can be analyzed to determine the failure characteristics of the structure under the action of large earthquakes.

CONFLICT OF INTEREST

Disclosure statement: on behalf of all authors, the corresponding author states that there is no conflict of interest.

AUTHOR CONTRIBUTIONS

Rujie Deng conducted data management, manuscript writing and software application; Xianqiao Meng and Shulin Zhang provided resources and funding for projects; Zhengliang Li conducted editing of the article, proofreading and data verification; all authors had approved the final version.

FUNDING

This research project was fully funded by China Energy Engineering Group Anhui Electric Power Design Institute Co., LTD. The authors would like to express their gratitude for all generous financial sponsorship.

REFERENCES

[1] K. Yang, L. Zhu, Y. Bai, et al, "Strength of external-ring-stiffened tubular X-joints subjected to brace axial compressive loading," *Thin-Walled Structures*, vol. 133, pp. 17-26, 2018.

[2] S. Z. Qu, G. H. Tang, J. Yuan, Q. G. Li, Q. Sun, J. T. Wang, "Study on synergistic mechanism of tube-gusset plate connections with multi-stiffened plates," *Thin-Walled Structures*, vol. 158, 2021.

[3] L. J. Zhang, S. C. Li, X. W. He, Z. W. Liu, Z. Y. Wang, "Study on effects of stiffening rings on bearing capacity and failure modes of large-diameter steel tube joints," *Industrial Construction*, vol. 51, no. 03, pp. 104-109, 2021.

[4] H. Kuwamura, H. Akiyama, "Brittle fracture under repeated high stresses," *Journal of Constructional Steel Research*, vol. 29, no. 1-3, pp. 5-19, 1994.

[5] A. M. Kanvinde, "Micromechanical simulation of earthquake-induced fracture in steel structures," Stanford University, 2004.

[6] J. R. Rice and D. M. Tracey, "On the ductile enlargement of voids in triaxial stressfields," *Journal of the Mechanics and Physics of Solids*, vol. 17, no. 3, pp. 201-217, 1969.

[7] A. M. Kanvinde and G. G. Deierlein, "Cyclic void growth model to assess ductile fracture initiation in structural steels due to ultra low cycle fatigue," *Journal of Engineering Mechanics*, vol. 133, no. 6, pp. 701-712, 2007.

[8] C. M. Smith, G. G. Deierlein, A. M. Kanvinde, "A stress-weighted damage model for ductile fracture initiation in structural steel under cyclic loading and generalized stress states," *Technical Rep*, vol. 187, 2014.

[9] W. Wang, F. F. Liao, Y. Y. Chen, "Ductile fracture prediction and post-fracture path tracing of steel connections based on micromechanics-bsaed fracture criteria," *Engineering Mechanics*, vol. 31, no. 03, pp. 101-108+115, 2014.

[10] Y. Yin, X. Y. Che, Q. H. Han, P. Lei, "Study on ultimate load bearing capacity of tubular XK-joints based on micromechanical fracture models," *China Civil Engineering Journal*, vol. 50, no. 07, pp. 20-26+121, 2017.

[11] A. G. Chen, K. M. Wang, J. H. Xing, Y. Chen, "Ductile fracture behavior of weld metal for Q345 steel under monotonic loading," *Engineering Mechanics*, vol. 37, no. 01, pp. 88-97, 2020.

[12] L. J. Jia and H. Kuwamura, "Ductile fracture simulation of structural steels under monotonic tension," *Journal of Structural Engineering*, vol. 140, no. 5, 2014.

[13] F. Liao, W. Wang, Y. Chen, "Parameter calibrations and application of micromechanical fracture models of structural steels," *Structural Engineering and Mechanics*, vol. 42, no. 2, pp. 153-174, 2012.

[14] B. L. Chen, "Fracture research of Q460C steel based on micromechanical damage models," M.S. thesis, Beijing Jiaotong University, 2017.

[15] Q0 Chen, "Research on the fracture behavior of high-strength circular steel tube materials based on micromechanical damage models," M.S. thesis. Beijing Jiaotong University, 2020.

[16] G. H. Shen, Z. Chen, Y. Guo, Y. L. Xing, B. N. Sun, "Bearing capacity of cross-shaped steel tubular joints with reinforced plate under brace compression," *Journal of Engineering Mechanics*, vol. 30, no. 09, pp. 70-75, 2013.

[17] F. F. Liao, R. Z. Wang, W. C. Li, T. H. Zhou, "Study on micro mechanism-based ductile fracture criteria for Q460 steel," *Journal of Xi'an University of Architecture & Technology (Natural Science Edition)*, vol. 48, no. 04, pp. 535-543+550, 2016.

[18] Y. Yin, X. F. Liu, Q. H. Han, Z. Liu, "Simulation of ductile fracture of structural steels with void growth model and a continuum damage criterion based on it," *Theoretical and Applied Fracture Mechanics*, vol. 98, 2018.

Copyright © 2023 by the authors. This is an open access article distributed under the Creative Commons Attribution License (CC BY-NC-ND 4.0), which permits use, distribution and reproduction in any medium, provided that the article is properly cited, the use is non-commercial and no modifications or adaptations are made.